remote sensing

MDPI

Article

Influence of Scattered Sunlight for Wind Measurements with the $O_2(a^1\Delta_g)$ Dayglow

Weiwei He [1], Xiangrui Hu [1], Houmao Wang [2], Daoqi Wang [1], Juan Li [3], Faquan Li [4] and Kuijun Wu [1,*]

1 School of Physics and Electronic Information, Yantai University, Yantai 264005, China
2 National Space Science Center, Chinese Academy of Sciences, Beijing 100190, China
3 Key Laboratory of Spectral Imaging Technology of Chinese Academy of Sciences, Xi'an Institute of Optics and Precision Mechanics, Chinese Academy of Sciences, Xi'an 710119, China
4 Innovation Academy for Precision Measurement Science and Technology, Chinese Academy of Sciences, Wuhan 430071, China
* Correspondence: wukuijun@ytu.edu.cn; Tel.: +86-166-5858-0859

Abstract: Observing the $O_2(a^1\Delta_g)$ dayglow with the limb-viewing DASH instrument enables remote sensing of neutral wind in near space. Many advantages are gained by using this new approach, but the influence factors on measurement accuracy have not been thoroughly investigated. This paper reports the quantitative evaluation of the wind error caused by scattered sunlight. The spectral concept of the $O_2(a^1\Delta_g)$ band and the measurement technique are briefly described. A comprehensive truth model simulation that is based on atmospheric limb radiance spectra and the instrument concept are used to obtain interferogram images. The algorithm, which uses these images to retrieve the interferogram containing information solely from the target altitude, is described. The self-absorption effect is taken into account in the unraveling of the line-of-sight integration. The influence of scattered sunlight on the limb-viewing weight and signal-to-noise ratio, two definitive factors for wind definitive factors, are also described. Representative wind precision profiles and their variation with surface albedo, aerosol loading, and cloud are presented. This indicates that the random error for Doppler wind is in the range of 2–3 m/s for the tangent height range from 45–80 km, and the wind precision under 45 km suffers significantly from scattered sunlight background.

Keywords: neutral wind; measurement accuracy; scattered sunlight; interferogram images

Citation: He, W.; Hu, X.; Wang, H.; Wang, D.; Li, J.; Li, F.; Wu, K. Influence of Scattered Sunlight for Wind Measurements with the $O_2(a^1\Delta_g)$ Dayglow. *Remote Sens.* **2023**, *15*, 232. https://doi.org/10.3390/rs15010232

Academic Editor: Stephan Havemann

Received: 14 November 2022
Revised: 20 December 2022
Accepted: 29 December 2022
Published: 31 December 2022

1. Introduction

The accuracy of Numerical Weather Prediction (NWP) is critically dependent on the quality and quantity of initial field information [1]. The development of a state-of-the-art variational data assimilation system enhances the precise quality of initial field information, but also leads to an urgent need for more meteorological observations on subsynoptic scales. Global wind field measurements become relatively more important than other meteorological parameters, such as mass or temperature, on these smaller scales [2].

Compared with mass or temperature observation, measuring the global wind field is much more difficult [3]. Current wind data can be obtained widely from conventional methods: direct balloon/rocket measurements, radars, RMR lidars, and simple Doppler lidars for local measurements [4] and indirect space-borne sensors, such as wind scatterometers [5] and cloud or water vapor tracking imagers [6]. However, these wind-measuring methods are limited in both altitude coverage and temporal or spatial resolutions.

The space-borne Doppler Wind Lidar (DWL) and Wind Imaging Interferometer (WII) are now widely regarded as the two potential ways to meet the global measurement requirements and fill the gaps limited by the mentioned methods above. ADM-Aeolus carried the first Doppler wind lidar into space in August 2018 for the observation of wind profiles on a global scale from the lower part of the troposphere to the lower part of the stratosphere (0 to 30 km altitude) [7]. MIGHTI, an instrument for remote sensing of the thermospheric neutral wind from 90 to 300 km by observing the Doppler shift of two naturally occurring atomic oxygen airglow emissions at 557.7 nm and 630.0 nm, is now orbiting Earth after a successful launch on October 2019 [8,9].

However, for the area comprised between 30 and 90 km of altitude, the so-called "near space", there are no space-borne sensors in orbit to provide 2D wind fields. Shepherd et al. designed the Stratospheric Wind Interferometer for Transport studies (SWIFT) instrument employing the method of Doppler–Michelson interferometry to measure stratospheric wind velocities in the altitude range of 15–45 km [10]. Gordley et al. presented a new approach, Doppler Wind and Temperature Sounder (DWTS), using gas filter radiometry, for measuring winds and temperatures from 25 to over 250 km [11]. Working in the Mid-Wave Infrared (MWIR) or Long-Wave Infrared (LWIR) wavebands enables SWIFT and DWTS to observe wind field day and night continuously, but at the same time causes problems of high instrument thermal backgrounds and great volume and leads to engineering difficulty in cryogenic cooling of the detector and instrument components. Supported by the Canadian Space Agency and the Centre for Research in Earth and Space Technology, William E. Ward et al. developed the Waves Michelson Interferometer (WAMI) to measure temperature and wind simultaneously from 45 to 95 km by observing three strong emission lines and three weak ones of the $O_2(a^1\Delta_g)$ dayglow with a Michelson interferometer [12]. More recently, Wu et al. reported the application of a Doppler-Asymmetric-Spatial-Heterodyne-spectroscopy (DASH)-type instrument for wind field measurements using a single emission line of the O_2 infrared atmospheric band as the target source, which reduced the design requirement spectral sampling interval and, thus, greatly increased the engineering feasibility [13]. Many advantages are gained by using this new method, but the novelty of this technique also means that the influence factors on the measurement accuracy remain unknown. Among a great numbers of influence factors, the spectral interference of scattered sunlight is the crucial factor for wind measurement precision.

Compared with the atmospheric band used by the Wind Imaging Interferometer (WINDII) [14], High Resolution Doppler Imager (HRDI) [15], and TIMED Doppler Interferometer (TIDI) [16], the infrared atmospheric band has greater advantages of bright signal and extended altitude coverage, which make it suitable for wind observing at a lower altitude (from about 30 km). However, the infrared atmospheric band can be observed both in emission and absorption at lower altitudes, and the weight of the emission signal decreases with the reduction of the altitude, which may lead to a reduction in wind measurement precision, especially at low altitudes [17]. In 2018, Wu et al. analyzed the influence of the spectral interference on the wind measurement, but only the Rayleigh scattering was taken into account [13]. However, the Mie scattering and the reflection of clouds and the Earth's surface also contribute significantly to the scattered sunlight continuum background, especially at low tangent heights [17].

In this paper, we carried out an overall and thorough research on the influence of scattered sunlight on wind measurements by using a limb-viewing DASH instrument to observe the $O_2(a^1\Delta_g)$ dayglow. A brief description of the spectral concept of the infrared atmospheric band is provided in Section 2. Section 3 presents the simulated interferogram images observed by the limb-viewing DASH instrument and describes how to unravel the Line-Of-Sight (LOS) integration to retrieve the interferogram containing information solely from the target altitude. Section 4 presents the wind measurement precision of the DASH instrument and discusses the effects of surface albedo, aerosol loading, and cloud. A concluding summary in Section 5 completes this paper.

2. Spectrum Spectral Concept

Measurements of the broadening and the frequency shift information of the airglow emissions with the satellite-borne Doppler imaging interferometer to observe the atmospheric wind of the high-altitude area have achieved great success. However, the extension of space coverage to lower altitudes, to some extent, greatly depends on the profound study of the spectroscopic information and radiation characteristics of the O_2 infrared atmospheric band, including the understanding of the production and loss mechanisms of the $O_2(a^1\Delta_g)$ state and recognizing the atmospheric scattering and absorption characteristics at 1.27 µm. Depending on the rotational energy level and atmospheric region, the O_2 lines in the infrared atmospheric band can be observed both in absorption and emission, the former dominating below about 40 km. It can be predicted that the influence of scattered sunlight on wind measurements by observing the $O_2(a^1\Delta_g)$ dayglow with a limb-viewing DASH instrument will increase with the reduction of altitude.

2.1. The $O_2(a^1\Delta_g)$ Photochemistry

Airglow refers to photon emissions through radiative deactivation of electronically excited molecules in the atmosphere. Spontaneous emissions of O_2 from the first excited state $a^1\Delta_g$ to the ground state $X^3\sum_g^-$ produce the 1.27 µm dayglow:

$$\mathrm{O}_2(a^1\Delta_g) \rightarrow \mathrm{O}_2(X^3\textstyle\sum_g^-) \; + h\upsilon(1.27\mu\mathrm{m}). \tag{1}$$

During the day, resonant phosphorescence by infrared solar radiation, the photolysis of O_3, and the energy transfer from $O(^1D)$ are three predominant mechanisms that produce O_2 molecules in their excited state $(a^1\Delta_g)$. The key photochemical processes that contribute to the production and loss of the $O_2(a^1\Delta_g)$ state are illustrated in Figure 1.

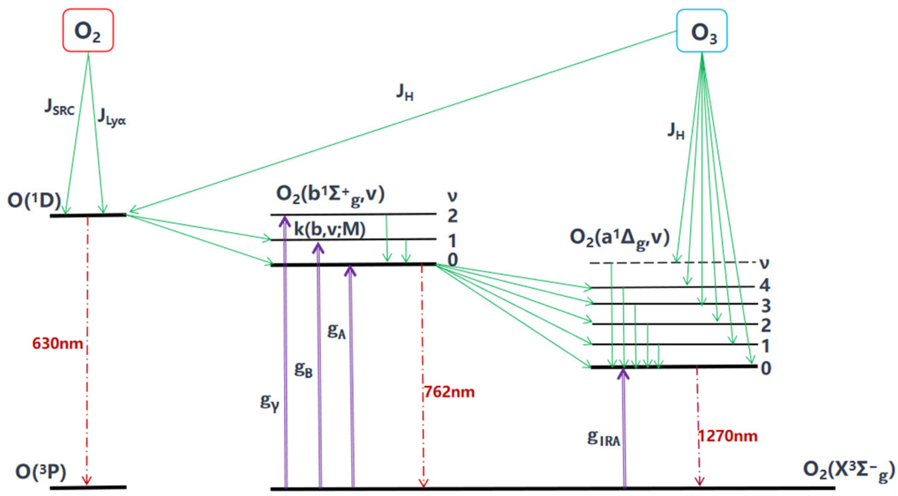

Figure 1. Production and loss mechanisms of the $O_2(a^1\Delta_g)$ state.

The photolysis of O_3 in the Hartley band results is the most-important mechanism in the production of $O_2(a^1\Delta_g)$ [18]:

$$\mathrm{O}_3 + h\upsilon(210 - 310\mathrm{nm}) \rightarrow \mathrm{O}_2(a^1\Delta_g) \; + \mathrm{O}(^1\mathrm{D}), \tag{2}$$

The resonant absorption of solar radiation in the A, B, and γ atmospheric bands (762, 688, and 629 nm) and the infrared atmospheric band (1.27 µm) also contributes significantly to the production of $O_2(a^1\Delta_g)$. Because the line intensity of the O_2 infrared atmospheric band is relatively weak, the photoexcitation-induced contribution from the 1.27 µm band is far from the dominant source of the $O_2(a^1\Delta_g)$ state, while resonant phosphorescence by the 762 nm band, which produces the O_2 $(b^1\sum_g^+)$ state, makes a relatively large contribution through quenching processes in collisions with all basic atmosphere components, especially for altitudes from 60 to 80 km. The O_2 $(b^1\sum_g^+)$ state interacts with other molecules and is quenched to the $O_2(a^1\Delta_g)$ state in collisional processes of energy transfer. The resonant excitation processes of the O_2 ($b^1\sum_g^+$) and $O_2(a^1\Delta_g)$ states, as well as the energy transfer of the O_2 ($b^1\sum_g^+$) state can be expressed by the following formulas:

$$\begin{aligned} &O_2(X^3\textstyle\sum_g^-)\ + hv(1.27\mu m) \to O_2(a^1\Delta_g) \\ &O_2(X^3\textstyle\sum_g^-)\ + hv(762nm) \to O_2(b^1\textstyle\sum_g^+) \\ &O_2(b^1\textstyle\sum_g^+)\ + M(=\ N_2, O_2, CO_2, O) \to O_2(a^1\Delta_g)\ + M \end{aligned}, \tag{3}$$

Energy transfer in the process of $O(^1D)$ reacting with O_2 also results in the formation of the excited $O_2(a^1\Delta_g)$ state with the energy transfer of the O_2 ($b^1\sum_g^+$) state:

$$\begin{aligned} &O(^1D) + O_2 \to O_2(b^1\textstyle\sum_g^+)\ + O(^3P) \\ &O_2(b^1\textstyle\sum_g^+)\ + M(=\ N_2, O_2, CO_2, O) \to O_2(a^1\Delta_g)\ + M \end{aligned}, \tag{4}$$

Taking the quenching processes in collisions with all basic atmosphere components such as N_2, O_2, CO_2, O_3, and $O(^3P)$ into account, the number density of $O_2(a^1\Delta_g)$ can be calculated by the following formula assuming photochemical equilibrium [13]:

$$n_{O_2(a^1\Delta_g)} = \frac{\phi_\alpha R_1[O_3] + \sum\limits_{i=1}^{5} K_i[Y_i]\frac{[O_2]\{R_2+\phi_\eta R_3[O(^1D)]\}}{A_{O_2(b^1\Sigma_g)}+\sum\limits_{i=1}^{5} K_i[Y_i]}}{A_{O_2(a^1\Delta_g)} + \sum\limits_{i=1}^{3} C_i[X_i]}, \tag{5}$$

where $X = \{O_2, N_2, O\}$, $Y = \{N_2, O_2, CO_2, O_3, O\}$, $0.54 < \phi_\eta < 1.0$, $K_1 = 2.1 \times 10^{-15}$, $K_2 = 4.2 \times 10^{-13}$, $K_3 = 2.2 \times 10^{-11}$, $K_4 = 8.0 \times 10^{-14}$, $K_5 = 3.9 \times 10^{-17}$, $C_1 = 3.6 \times 10^{-18} e^{-220/T}$, $C_2 = 1.0 \times 10^{-20}$, $C_3 = 1.3 \times 10^{-16}$, $R_1 = 8.1 \times 10^{-3}$, $R_2 = 5.35 \times 10^{-9}$, and $R_3 = 3.2 \times 10^{-11}\exp(70/T)$.

The amounts of the O_2 ($a^1\Delta_g$) state attributable to each of the production mechanisms discussed above are shown in Figure 2. All values of the rate constants including photodissociation and photoexcitation processes were taken from the work of Yankovsky et al. [19,20]; the transition probability $A_{O_2(a^1\Delta_g)}$ was calculated based on the HITRAN 2016; the profiles of O, O_2, N_2, and CO_2 were obtained from the atmosphere model of NRLMSIS [21]. The individual contributions from each of the production and loss mechanisms are described and marked in the figure legend.

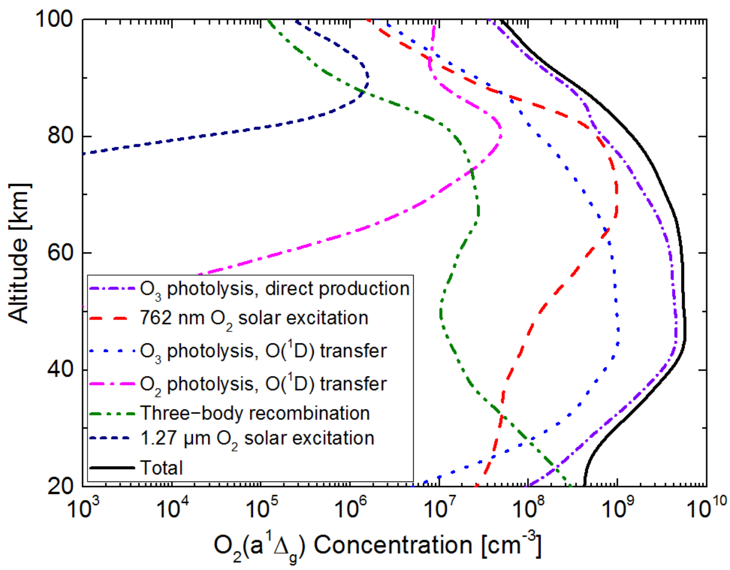

Figure 2. Calculated $O_2(a^1\Delta_g)$ concentration profiles for different production mechanisms.

The Volume Emission Rate (VER), which represents the number of photons emitted per unit volume per unit time from the excited state to the ground one with radiative relaxation, can be calculated by weighting the transition probability of the $O_2(a^1\Delta_g)$ state with its number density:

$$\eta_E(s) \ = \ A_{O_2(a^1\Delta_g)} \cdot n_{O_2(a^1\Delta_g)}(s), \tag{6}$$

Among the $O_2(a^1\Delta_g)$ state production processes, all but the three-body recombination mechanism are strongly affected by the solar radiation, especially for the calculation of the photodissociation rate of O_2 and O_3 and resonant absorption of O_2. The change of the Solar Zenith Angle (SZA) leads to the variation of the pathlength that the solar radiation passes through the absorber species (such as O_2 or O_3), which, in turn, causes a change in the photochemical coefficients and resonant absorption efficiency. Therefore, the number density of $O_2(a^1\Delta_g)$ is very strongly modulated by the SZA. The $O_2(a^1\Delta_g)$ VER profiles for different SZAs from 0° to 90° were calculated using fixed ozone profiles obtained from Modtran [22] and shown in Figure 3. It is well known that the profile of O_3 concentration has a large solar local time and SZA variations. Therefore, the simulated $O_2(a^1\Delta_g)$ VER from the O_3 photolysis source may have some errors due to the assumption of O_3 concentration invariance. However, it does not matter for the discussion of the features apparent in this figure. The intensity of the $O_2(a^1\Delta_g)$ emission reaches its maximum at local noon with a peak systematically appearing at 43 km to 45 km for values of the SZA below 50°. This peak rises with the SZA because the solar radiation passes through a longer O_3 column when the Sun nears the horizon, which decreases the production by the photolysis reaction of O_3 in the lower altitude region.

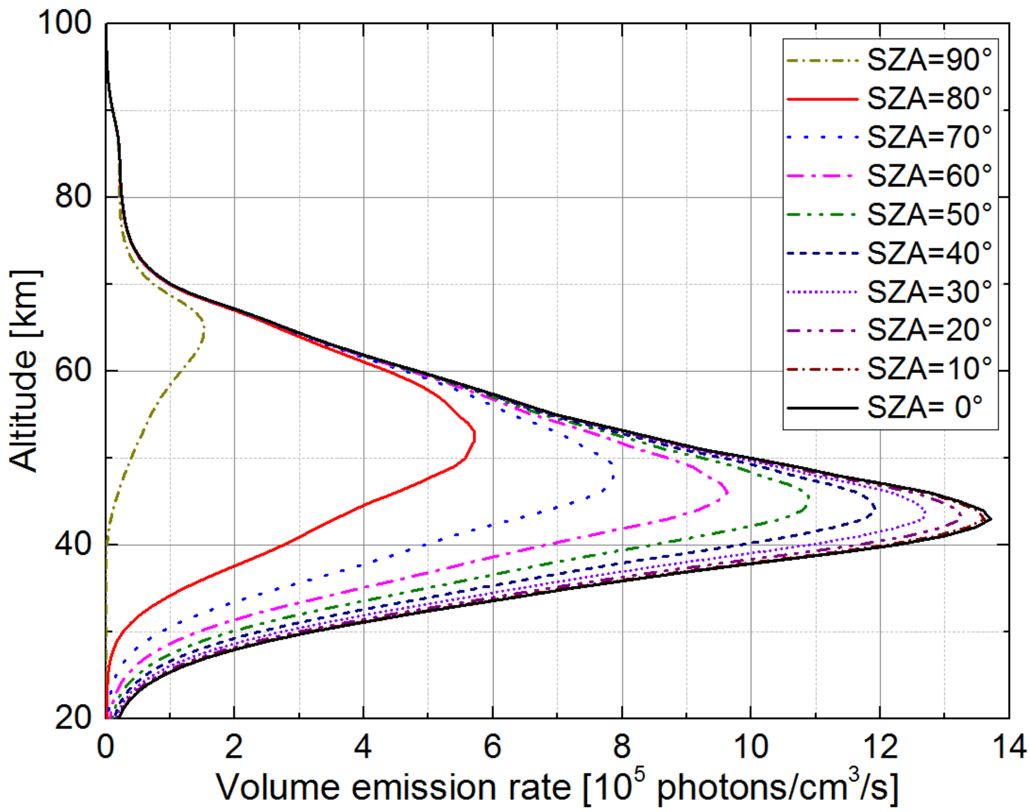

Figure 3. Calculated VER profiles of O_2 airglow at 1.27 μm. Ten profiles were drawn at SZAs from 0° to 90° with an interval of 10°.

2.2. Limb Radiation Spectrum of $O_2(a^1\Delta_g)$

The infrared atmospheric band (1.27 μm) of O_2 is characterized by two P branches and two R branches due to a series of rotational distributions attributed to the transition $O_2(a^1\Delta_g, v' = 0) \to O_2(X^3\Sigma_g, v'' = 0)$. The spectral distribution of $O_2(a^1\Delta_g)$ depends on the individual rotational statistical weight $2J + 1$ and the temperature T.

The emission rate per $O_2(a^1\Delta_g)$ with rotational number J can be calculated by multiplying the transition probability $A_{O_2(a^1\Delta_g)}$ by its actual distribution:

$$\varepsilon_J = A_{O_2(a^1\Delta_g)} \cdot \frac{Q(J,T)}{\sum Q(J,T)}, \tag{7}$$

The relative population of the rotational transition J can be computed from:

$$Q(J,T) = (2J+1)\exp(-\frac{hcE_J{}'}{k_B T}), \tag{8}$$

where $E_J{}'$ is the lower-state energy, h is the Planck constant, c is the speed of light, and $k_B = 1.38065 \times 10^{-23}$ J/K is the Boltzmann constant.

Figure 4 shows the emission spectrum of the $O_2(a^1\Delta_g)$ band as a function of the transition wavelength at two different values of temperature, 100 K and 400 K. As can be seen, the radiation intensity decreases at the center of the band while the wing increases.

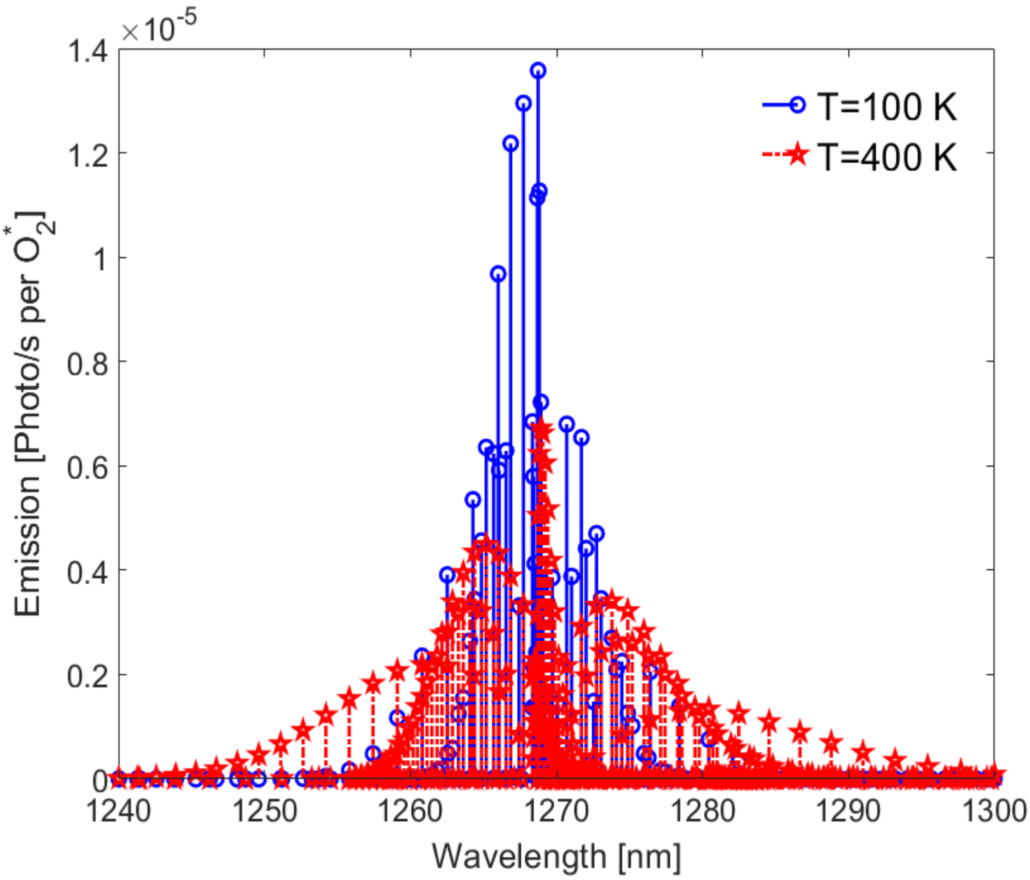

Figure 4. The emission spectrum of the $O_2(a^1\Delta_g)$ band as a function of the transition wavelength.

For limb measurements without self-absorption, the spectral brightness can be treated as a straightforward Abel-type integration of the VER along the LOS path. However, for the $O_2(a^1\Delta_g)$ band, the calculation of spectral brightness becomes difficult for a tangent altitude below 60 km, where the self-absorption effect is strong and cannot be ignored. For the accurate simulation of the observed $O_2(a^1\Delta_g)$ band spectral brightness, interference from the upper layers due to self-absorption must be taken into account in the calculation of the VER path integrals. The VER of any rotation line J at a point along the LOS can be denoted as η_J, and the spectral brightness of this rotational line as a function of wavenumber v can be written as [17]:

$$B_e(v - v_J) = \int_{z_t}^{obs} \eta_E(J,s) \mathrm{D}(v - v_J + \Delta v) \times \exp(-\int_{z_t}^{obs} n(s')\sigma_J \mathrm{D}(v - v_J + \Delta v) ds'), \quad (9)$$

where $\eta_E(J,s) = \varepsilon_J \cdot n_{O_2(a^1\Delta_g)}(s)$, n is the number density of the ground state O_2, σ_J is the absorption cross-section of the given rotation line J, and $\mathrm{D}(v - v_J + \Delta v)$ is the line shape at position s and shifted by the atmospheric wind V along the LOS with $\Delta v = v_J V/c$.

Figure 5a,b show the simulated limb spectral brightness of the $O_2(a^1\Delta_g)$ band at tangent heights of 50 km and 70 km. For comparison, the spectral line brightness calculated by using the straightforward Abel-type integration with the self-absorption neglected is also shown. Figure 5c shows the ratio of spectral line brightness with and without considering the self-absorption effect, which clearly shows that, in the area above 60 km, the self-absorption effect can be ignored. As illustrated, the self-absorption is significant at a 50 km tangent height and is important up to 60 km for the $O_2(a^1\Delta_g)$ band. The amount of absorption, or in other words, the effective optical depth, is hugely dependent on the O_2 density along the LOS. Because the absorption cross-section is the largest at the center and decreases toward the wings, either for a single line or for the whole band, the temperature deduced from the line shape of the single line or from the rotational structure of the whole band will be larger than the kinetic temperature. The rotational lines in two wings of the $O_2(a^1\Delta_g)$ band are optically thin and suffer little from self-absorption. Therefore, the emission lines in those attractive wavelength regions provide the most-accurate means of detecting temperature or wind.

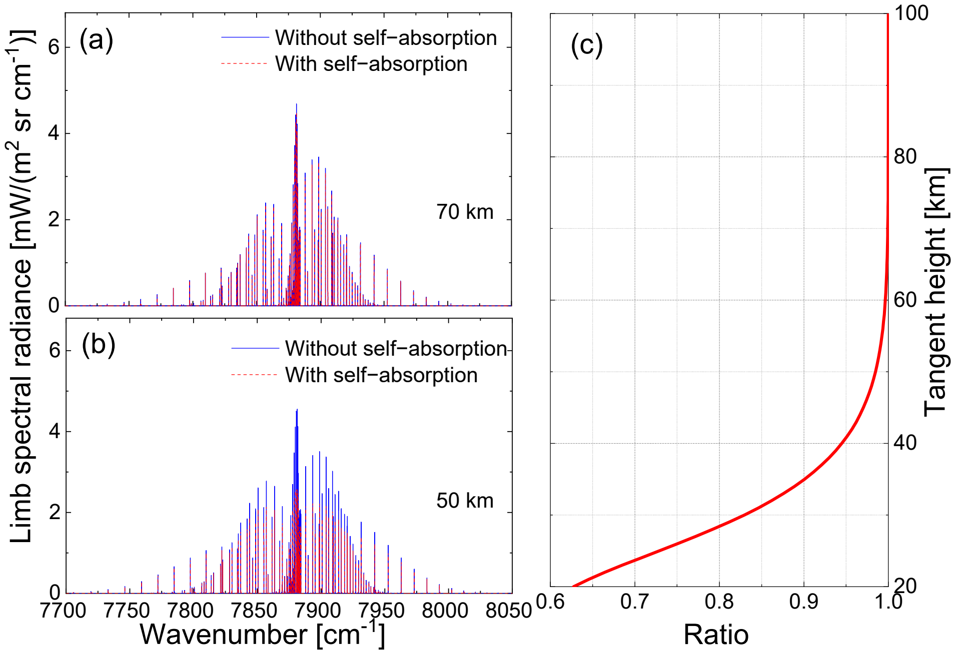

Figure 5. (**a**) The simulated limb spectral brightness of the $O_2(a^1\Delta_g)$ band at a tangent height of 70 km (with and without the effect of self-absorption); (**b**) the simulated limb spectral brightness of the $O_2(a^1\Delta_g)$ band at a tangent height of 50 km (with and without the effect of self-absorption); (**c**) the ratio of spectral line brightness with and without considering the self-absorption effect.

2.3. Scattering Absorption Spectrum

The spectral signal obtained by the limb-viewing mode comes from two parts, airglow radiation and atmospheric scattering. The atmospheric scattering includes Mie scattering and Rayleigh scattering. Moreover, the spectrum of atmospheric scattering will carry the vibration rotation spectrum information of atmospheric molecules due to the absorption of atmospheric molecules during the scattering process of the solar spectrum. In the visible region, Rayleigh scattering by gas molecules or Mie scattering by aerosols is the primary cause of the light scattering. The sunlight background scattered by aerosol and atmospheric molecules plays a key role in the spectral interference for limb observation of the $O_2(a^1\Delta_g)$ dayglow, especially at low tangent heights. The scattered spectrum of the atmosphere is determined by the physical characteristics of absorbing species, individual scattering, and the optical properties of the surface, which make up the optically active components of the scattering process.

If we denote the volume scattering rate at a point s along the LOS by η_R for Rayleigh and η_M for Mie, the spectral brightness of atmospheric scattering B_s can be written as [23]:

$$B_s(v) = \int_{z_t}^{obs} [\eta_R^s(v) + \eta_M^s(v)] \times \exp(-\int_{z_t}^{obs} n(s')\sigma_J \mathrm{D}(v - v_J + \Delta v)ds'), \quad (10)$$

where the scattering rate per unit volume can be calculated using $\eta_{R,M}^s(v) = n_t F_s(v) P_{R,M}(\phi)\beta_{R,M}(v)$. Here, $P_{M,R}(\phi)$ is the Mie or Rayleigh phase function at scattering angle ϕ, $\beta_{R,M}(v)$ is the total Rayleigh or Mie scattering cross-section at frequency v, F_s is the top-of-atmosphere solar spectral irradiance, and n_t is the total atmospheric density.

In this scattering model, the light scattered by the atmosphere is taken into account on the assumption that it comes directly from the Sun or the reflection by the ground or the clouds with a simple Lambertian boundary characterized by a single albedo. The brightness reflected by the ground or the clouds can be given by:

$$B_R(v) = 4R_0\cos(\alpha_0)F_s(v)\exp\left(-\frac{\tau(0,v)}{\cos(\alpha_0)}\right), \quad (11)$$

where R_0 is the albedo, α_0 is the SZA, and $\tau(z,v) = \int_z^\infty n(z')\sigma(v)\mathrm{D}(v)dz'$ is the atmospheric transmittance.

The volume scattering rate at the scattering altitude due to the contribution of the ground or the cloud reflection can thus be expressed as:

$$\eta_G^s(v) = \frac{F_s(v)R_0\cos(\alpha_0)}{\pi}n(z)\int_0^{2\pi}\int_0^{\pi/2}\beta_{R,M}(v)\mathrm{P}(\delta)\exp\left(-\frac{\tau(0,v)}{\cos(\alpha_0)} - \frac{\tau(0,v)-\tau(z,v)}{\cos(\varphi)}\right)\sin(\varphi)d\varphi d\delta, \quad (12)$$

Figure 6 shows the spectral brightness of the limb atmospheric scattering of the $O_2(a^1\Delta_g)$ band at the tangent height of 35 km for different situations of aerosol, albedo, and cloud. It is widely known that the rotational lines are strongly pressure-broadened at lower altitudes and are broadened only by the Doppler effect at higher altitudes; thus, the line shape varies sharply with altitude. A Voight line profile was adopted in this work. As can be seen from Figure 12, the limb spectral brightness of atmospheric scattering is strongly dependent on the atmospheric conditions. The scattering spectral intensity increases fivefold to sixfold under cloudy and/or aerosol loading conditions.

As also can be seen from the comparison between Figures 5 and 6, the O_2 absorption spectrum is quite similar to the O_2 * emission spectrum. However, there are several factors that make them different in their spectral profile. Firstly, the line shape of the absorption spectrum is wider than the emission line because the Doppler broadening dominates at high altitudes. Secondly, the collision-induced absorption occurs in the scattering spectrum, but not in the airglow spectrum due to the fact that the effect of collision-induced absorption is proportional to the square of the O_2 density and, therefore, can be neglected at high altitudes. Thirdly, the absorption is not linear when $\tau > 1$, while the emission remains linear.

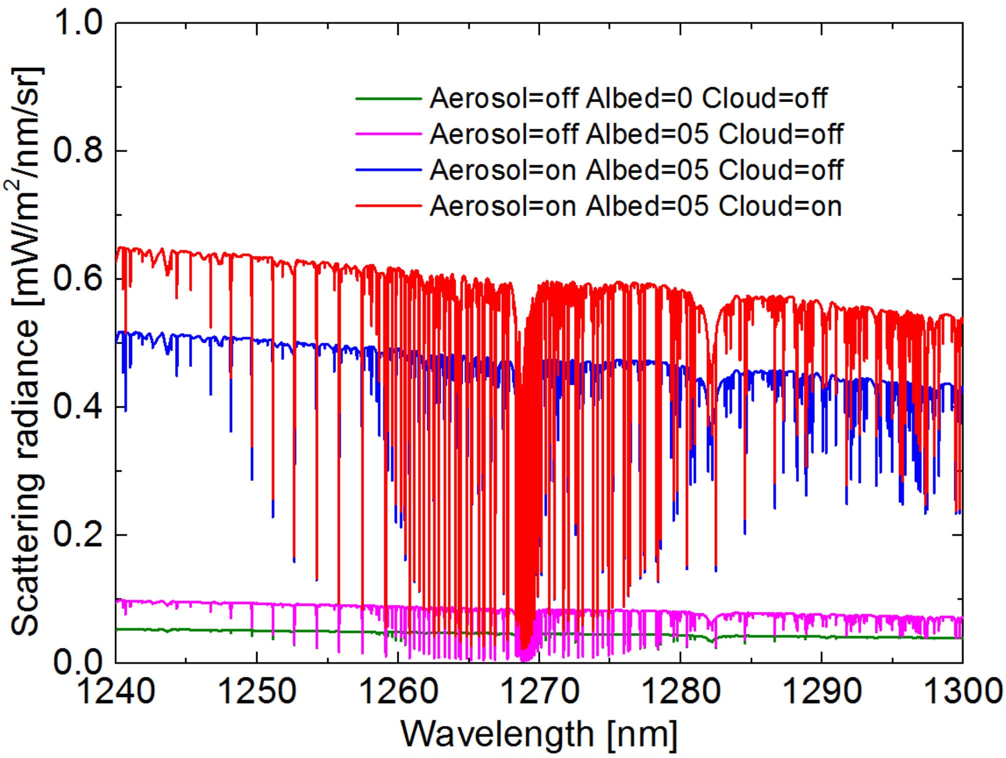

Figure 6. The spectral brightness of the limb atmospheric scattering at the tangent height of 35 km for different situations of aerosol, albedo, and cloud.

The atmosphere parameters used in this limb atmospheric scattering model were synthesized from the MSIS model, and the scattering cross-sections of the aerosol scattering are those appearing in the MODTRAN [22]. The phase function of Mie scattering was generated using the standard Mie scattering theory for spherical particles. The major difficulty in computing the limb spectral brightness is the effects of multiple scattering; to deal with this, the spherical adding and doubling methods reported by Abreu et al. were adopted in this work. The parameters of interest are listed in Table 1.

Table 1. Atmospheric conditions for limb atmospheric scattering simulations.

Feature		Description
Boundary layer	Albedo	0.5
	Aerosol type	rural
	Visibility	23 km
	Humidity	70%
Troposphere	visibility	50 km
	humidity	70%
Cloud	Sub-layers' number	10
	Thermodynamic state	water
	Liquid water path	500 g/m^2
Viewing geometry	Solar zenith angle	60°
	Azimuthal angle	0
	Tangent height	35 km

2.4. Limb Spectral Radiance

The infrared atmospheric band is ideally suitable for remote sensing of global 2D wind fields in near space due to the fact that it provides the best spectral features in the visible and near-infrared regions from 30 to 90 km [4]. Depending on the tangent height, the infrared atmospheric band can be observed both in emission and absorption, and the latter dominates at low altitudes. Since the emission and scattering processes are relatively independent of each other in both physical models and mathematical algorithms, the total spectral radiance can be obtained by adding these two components together. As previously mentioned, the VER of the $O_2(a^1\Delta_g, \nu' = 1 \rightarrow \nu'' = 0)$ emission band is denoted as $\eta_E(s)$ (in photons/cm^3/s) and the atmospheric volume scattering rate per wavenumber as $\eta_S(s)$(in photons/cm^3/s/cm^{-1}); thus, the total spectral radiance L_{Total} of one rotational line with the center frequency at v_i as a function of wavenumber v can be written as:

$$\begin{aligned} L_{Total}(v) &= \int_{-\infty}^{obs} \left[\eta_E(s) f_i(s) \mathrm{D}(v - v_J + \Delta v, s) + \eta_R^s(s) + \eta_R^s(s) + \eta_G^s(s)\right] \\ &\quad \times \exp\left[-\int_s^{obs} n(s')\sigma_J(s')\mathrm{D}(v - v_J + \Delta v, s')ds'\right] ds \end{aligned}, \tag{13}$$

where $f_J(s)$ and $\sigma_J(s)$ are the relative emission line strength and absorption cross-section of a point along the LOS s for the rotation line J. Note that $\eta_E(s) f_i(s) \mathrm{D}(v - v_J + \Delta v, s)$ is the airglow emission component, and $\eta_R^s(s)$, $\eta_M^s(s)$, and $\eta_G^s(s)$ are the atmosphere scattering component for Rayleigh, Mie, and reflection by the ground or the cloud. The calculation of the $O_2(a^1\Delta_g)$ VER can be solved with the YM2011 model (a complete model for electronic vibrational kinetics of O_2 and O_3 photolysis products developed by Yankovsky et al. [18,24])

Figure 7 shows the limb spectral radiance of the $O_2(a^1\Delta_g)$ band as a function of the tangent height. The emission lines are found to peak from 40 km to 70 km with slow declines above and below their peaks. The scattering spectrum is strongly marked by rotational lines, and its intensity increases exponentially as the altitude goes down. The emission line of $O_{19}P_{18}$ (7772.030 cm^{-1}) takes great advantage of the relatively larger spectral separation range, which makes it the optimum candidate line for the limb-viewing DASH instrument, because of its low requirement for the spectral sampling interval [13].

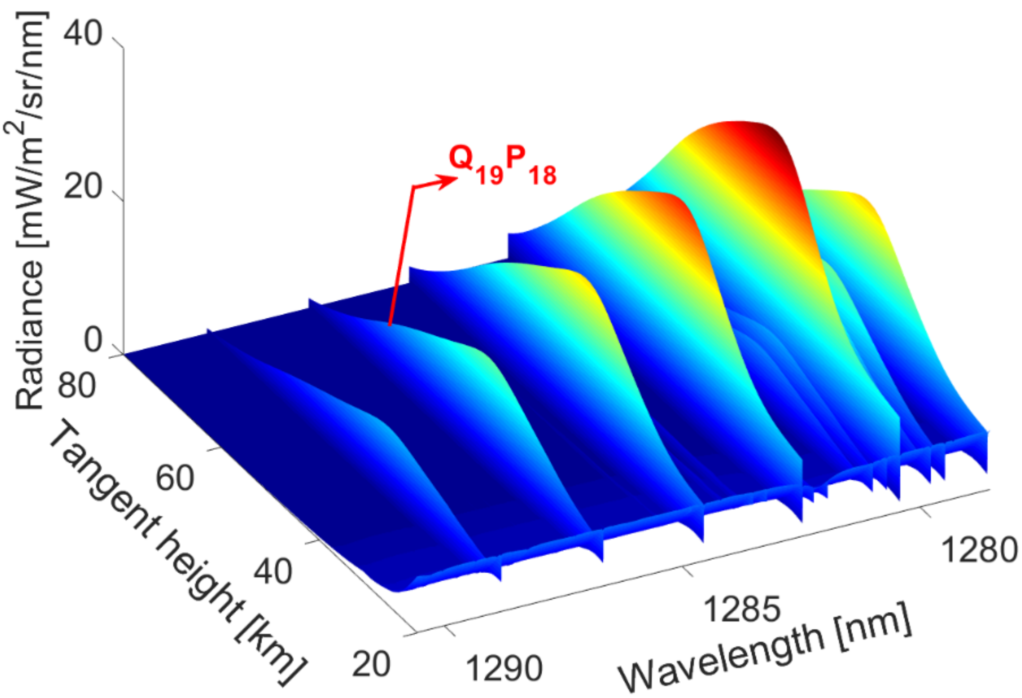

Figure 7. The limb spectral radiance of the O_2 infrared atmospheric band as a function of tangent height.

The surface albedo, aerosol loading, and cloud have a significant influence on the radiative transfer characteristics of the $O_2(a^1\Delta_g)$ band in the limb-viewing geometry [17]. Figure 8 shows the radiance variations of the O_2 line $O_{19}P_{18}$ with aerosol, albedo, and cloud. The wavelength (from 1286.63 to 1286.70 nm) is the abscissa; the tangent height (from 20 to 100 km) is the ordinate; the scale of the spectral brightness in each graph is made by the pseudo color intensity at the right edge. In the case of pure Rayleigh scattering (an ideal case by ignoring the aerosol scattering and the ground and cloud reflection), the asymptotic value (in the wings of the resonance line) at 20 km is one order of magnitude smaller than that of the line center intensity, as shown in Figure 8a. For the case of taking the atmospheric aerosol (with an aerosol model of stratospheric background and visibility of 10 km) into account, the asymptotic intensity increases by approximately six-times the case of pure Rayleigh scattering (see Figure 8b). If the ground albedo is set equal to 0.5 rather than 0, the asymptotic value doubles its intensity (see Figure 8c). This value adds another 150 percent in the presence of cloud (shown in Figure 8d). The intensity of the line center is less affected by the value of surface albedo, aerosol loading, or cloud. This behavior is due to the fact that the line center intensity depends largely on the VER profiles of the $O_2(a^1\Delta_g)$ dayglow. The change of the extinction coefficient caused by the existence of aerosol may lead to a slight variation in the center intensity, but the extinction effect of Mie scattering is far from obvious at altitudes above 20 km.

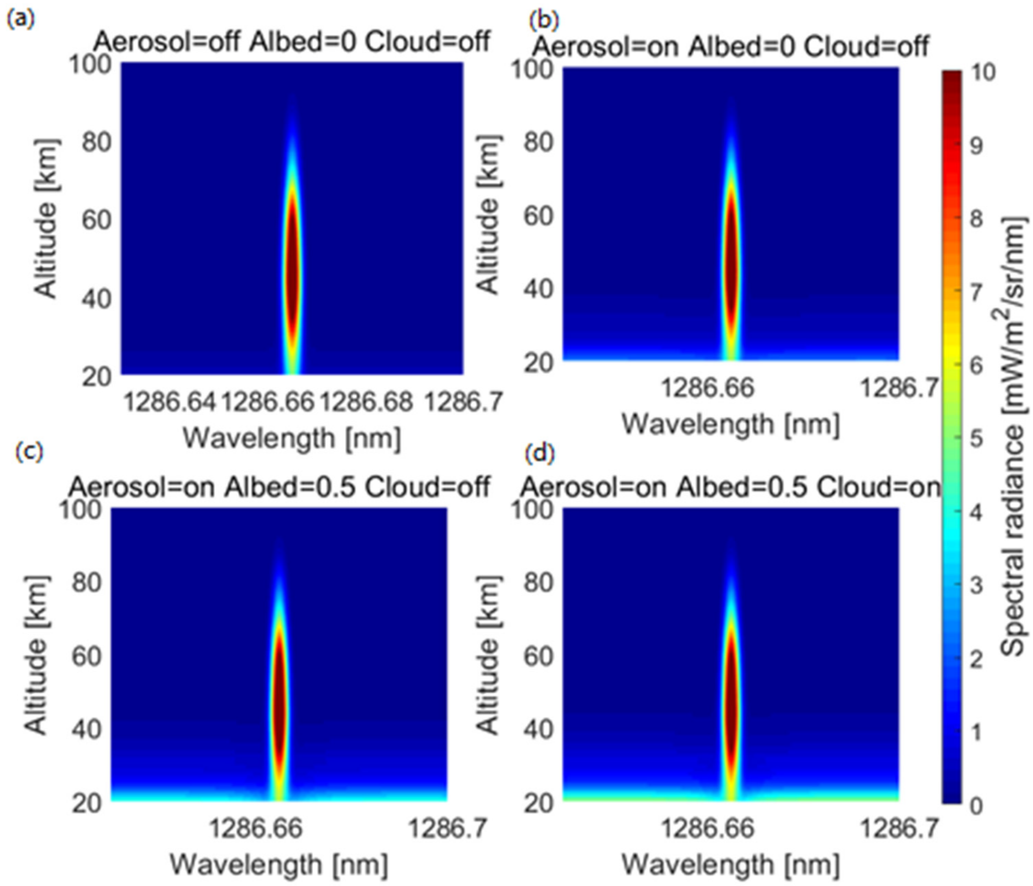

Figure 8. The radiance variations of the O_2 line $O_{19}P_{18}$ with aerosol, albedo, and cloud at tangent heights from 20 to 100 km.

3. Interferogram Image Inverting

3.1. Viewing Geometry

For actual limb viewing, different layers of the Earth's atmosphere contribute to the signal line in the interferogram, and the atmospheric composition of each layer is different. Therefore, both forward simulation and retrieval algorithms must consider the parameters of each layer in the direction of the LOS. The limb radiation radiance observed by the satellite is the path integral along the LOS from the height of the tangent point, and the radiation intensity of each layer is obtained by pointing the LOS to the tangent direction at different heights. Figure 9 shows the limb viewing geometry of the satellite.

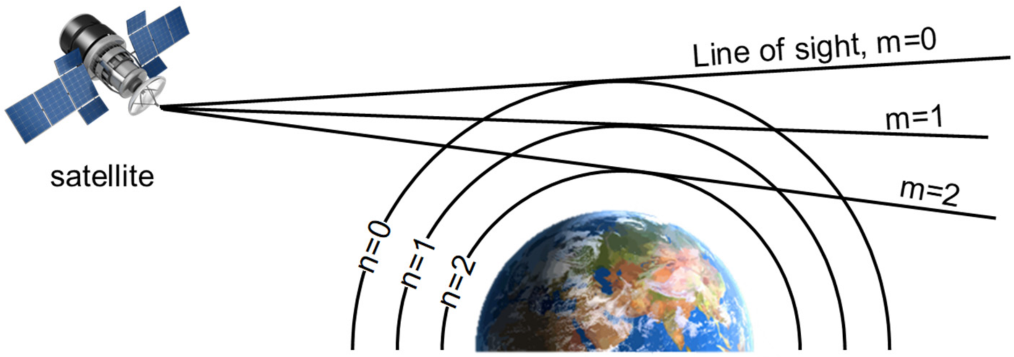

Figure 9. Limb viewing geometry of satellite.

3.2. Instrument Concept and Forward Model

The DASH instrument consists of a Michelson interferometer with tilted, fixed diffraction gratings in the two arms. In order to maximize the sensitivity to Doppler shift, an additional optical path offset is introduced in one arm [25]. A wavenumber-dependent Fizeau fringe pattern is recorded by the detector array because of the tilt of the wavefronts caused by the gratings. The Fourier transform of the incident light with a complex spectrum produces a spatial fringe frequency [26]. The relationship between the interferogram recorded by the DASH array detector and the observed spectrum is [13]:

$$H(x) = \frac{1}{2}\int_0^\infty L(v)T(v)[1+\cos\{2\pi[4(\nu-\nu_L)\tan\theta_L x + 2\nu\cdot\Delta d]\}]d\nu, \quad (14)$$

where $L(v)$ is the atmospheric spectral radiance, $T(v)$ is the transmission function of the filter, $\nu_L = 1/(2g\sin\theta_L)$ is the Littrow wavenumber (θ_L is the Littrow angle of the gratings, and $1/g$ is the groove density of the gratings), x is the location on the detector array corresponding to the Optical Path Difference (OPD), and $2\Delta d$ is the additional OPD offset in one of the interferometer arms.

The raw interferogram image recorded by the limb-viewing DASH instrument contains two main contributors: the $O_2(a^1\Delta_g)$ dayglow emission and the scattered sunlight background. It is indisputable that the airglow emission generates an ideal interferogram, while the scattered sunlight with a quasi-continuous spectrum produces a constant background, which is superimposed on the interference fringe. According to Harding [27], the first step in processing the original LOS-integrated interferogram is to remove the DC value (i.e., non-modulated term).

The raw interferogram image recorded by the DASH instrument is shown in Figure 10a. The DASH technique was developed specifically to measure atmospheric winds while simultaneously monitoring calibration signals to monitor instrument drifts. The brightness and fringe contrast of the interferogram include information about the density of the emitter and the line shape. The phase shift, $\delta\varphi$, of a single emission line can be obtained by the following equation:

$$\delta\varphi = 4\pi\Delta d\sigma(s/c) = 2\pi k(s/c) \quad (15)$$

where σ is the non-Doppler-shifted wavenumber of the emission line, s is the Doppler velocity, and c is the speed of light.

The atmospheric wind field profile used in Figure 10 was taken from the Horizontal Wind Model updated by the U.S. Naval Research Laboratory [28]. The corresponding specifications were taken from Table 1 of [13]. The vertical axis in each subgraph contains altitude information (from 30 to 90 km); the horizontal axis contains spectral information; the fringe pattern along the horizontal axis of the focal plane array (FPA) corresponds to a varying optical path difference (from 3.5 to 6.5 cm). Three major noise sources, including shot noise, readout noise, and detector dark noise, were taken into account in the simulation of the interferogram images. The noise was simulated using a random Gaussian deviation. For the interferogram shown in Figure 10a, it includes not only the airglow signal, but also the atmospheric scattering background, as there is no perfect blocking of the radiation spectrum within the passband of the filter, so it is referred to as the combined signal.

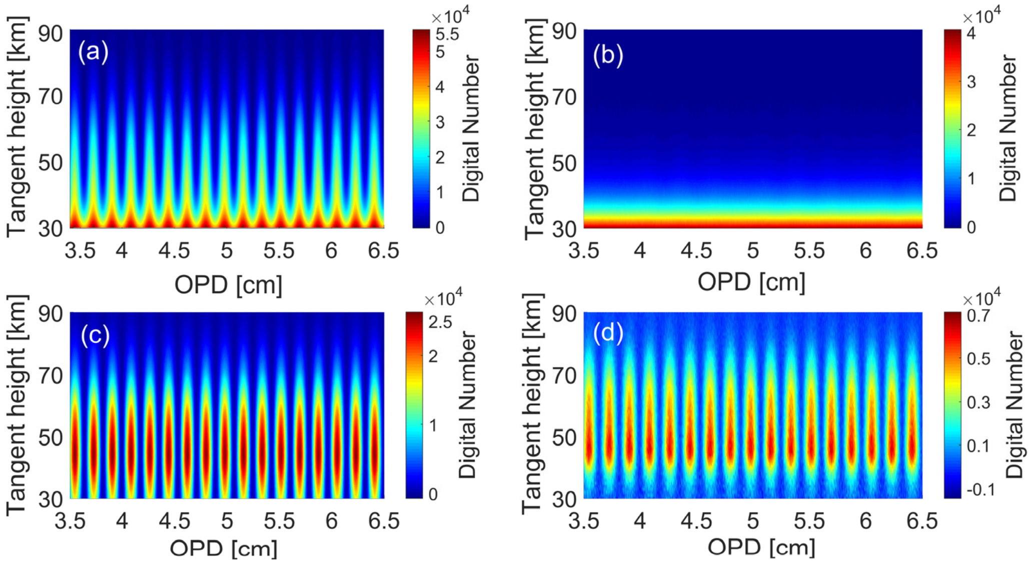

Figure 10. The process of retrieving the interferogram containing information solely from the target altitude. (**a**) The combined signal image (sum of airglow emission and scattering atmospheric signals) with noise added; (**b**) the scattering atmospheric signal image; (**c**) the recovered (scattering signal subtracted) atmospheric signal image; (**d**) the recovered atmospheric signal image after unraveling the LOS integration.

Figure 10b shows the atmospheric scattering signal image, which was obtained by only using the scattered sunlight background as the input for the atmospheric spectral radiance $L(v)$ in Equation (2). A comparison between the two images shows that the combined signal is dominated by the atmospheric scattering signal below 40 km, as would be expected for limb-viewing instruments. In an actual observation, each row of the interferogram contains contributions from $O_2(a^1\Delta_g)$ dayglow emission and the scattered sunlight background, especially for low altitudes. The non-modulated term of the interferogram can be simply removed by using straightforward Fourier techniques [29].

The process of retrieving the interferogram containing information solely from the target altitude is shown in Figure 10c,d. Figure 10c shows the recovered (scattering signal subtracted) atmospheric signal image, in which each row contains the contributions from many different layers characterized by different winds, temperatures, and volume emission rates. The inverted interferogram containing information solely from the target altitude is shown in Figure 10d.

3.3. Interferogram Image Inverting

The upgraded interferogram inverting technique, previously developed for MIGHTI, was adopted here [27]:

$$\begin{aligned} I_0(x)e^{j\Delta\varphi_0} &= \frac{1}{\omega_{00}}H_0(x) \\ I_m(x)e^{j\Delta\varphi_m} &= \frac{1}{\omega_{mm}}\left[H_m(x) - \sum_{n=0}^{m-1} I_n(x)e^{j\Delta\varphi_n \cos\alpha_{mn}}\omega_{mn}\right] \end{aligned}, \quad (16)$$

where I_m is the interferogram of the mth row of FPA, $\Delta\varphi_n$ is the phase shift caused by the horizontal wind of the nth layer, α_{mn} is the angle between the horizontal plane and the mth LOS at the intersection with the nth layer, and ω_{mm} is the weight of the LOS m at altitude n.

It is worth pointing out the major conceptual differences between the inversion used for MIGHTI and the inversion for our instrument. For MIGHTI, the retrieval assumes that the weights determined by the summation rule used to approximate the integral are spherically symmetric. However, this is not practicable for the DASH instrument using the $O_2(a^1\Delta_g)$ airglow as the detection object due to the presence of the self-absorption effect. The self-absorption process of O_2 molecules in the ground state must be taken into account when unraveling the LOS integration.

The signal-to-noise ratio (SNR) and the limb-viewing weight work together to determine the precision of wind measurement. The contribution rate profile of the pure emission atmospheric signal in the combined signal and the limb-viewing weight (the ratio of the unraveled atmospheric signal to the integral along the LOS) profile are shown in Figure 11a. The effective SNR, defined as the ratio of the atmospheric signal to the measurement noise from the combined signal images, is shown in Figure 11b. As is apparent, the contribution rate of $O_2(a^1\Delta_g)$ emission comes into prominence as the altitude increases. The limb-viewing weight also increases with the increase of the altitude. The effective SNR profile was found to peak around 45 km with slow declines above and below this peak. The very small values of the SNR at high and low tangent heights are because of the very weak VER at these tangent heights.

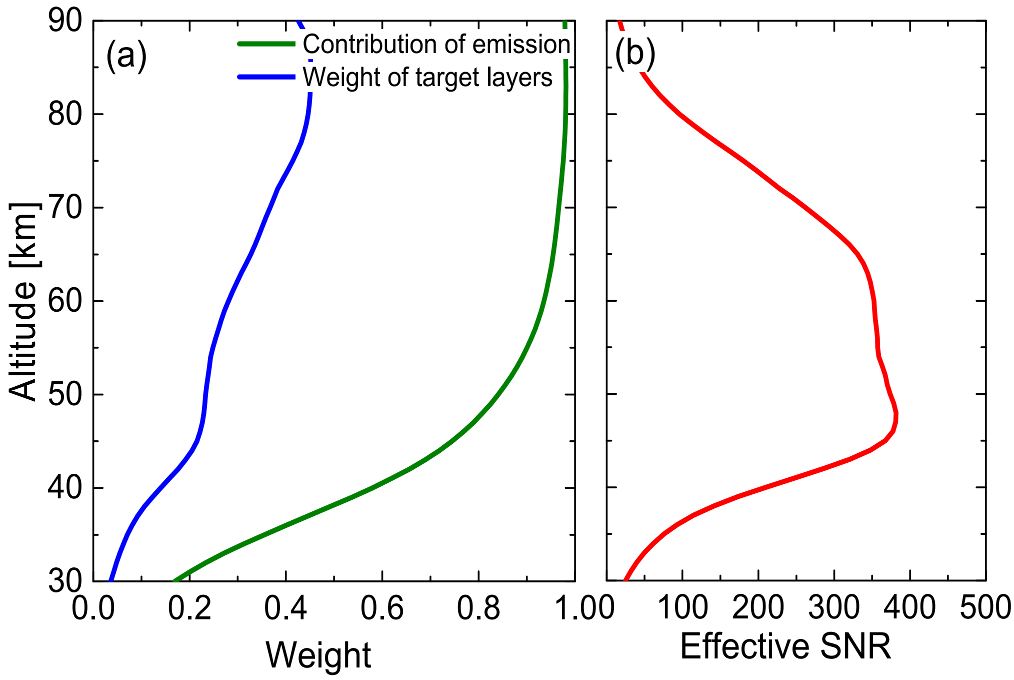

Figure 11. The limb-viewing weight and the contribution rate of the pure emission atmospheric signal (**a**) and the effective SNR; (**b**) varying with tangent altitude.

4. Measurement Error Evaluation

The retrieval approach of the wind signals was based on the optimal estimation concept, where the measurement sensitivity estimate plays a significant role. The measurement sensitivity can be determined from the propagation of errors. The noise propagation from the measured interferogram to the retrieved phase was described by Englert et al. in detail [25]. The sensitivity analysis is also practicable by following [30] and [31], with the simulations of combined atmospheric signals shown in Figure 8. The wind error is a function of the effective SNR, which, for $O_2(a^1\Delta_g)$ dayglow emission at altitudes of >50 km, is strongly dependent on the time of day and solar activity, while for altitudes of <50 km, it is determined by the ratio of the pure emission atmospheric signal to the combined one.

For the error study, modeling the signal for a hypothetical limb-viewing DASH instrument (with the specifications the same as used in the simulation of Figure 10) must be performed. The variations of the calculated signal images with different aerosol loading, surface albedo, and cloud are shown in Figure 12. The simulations indicate that the presence of the spectral interference of the scattered sunlight background decreases the interferogram contrast and increases the measurement noise.

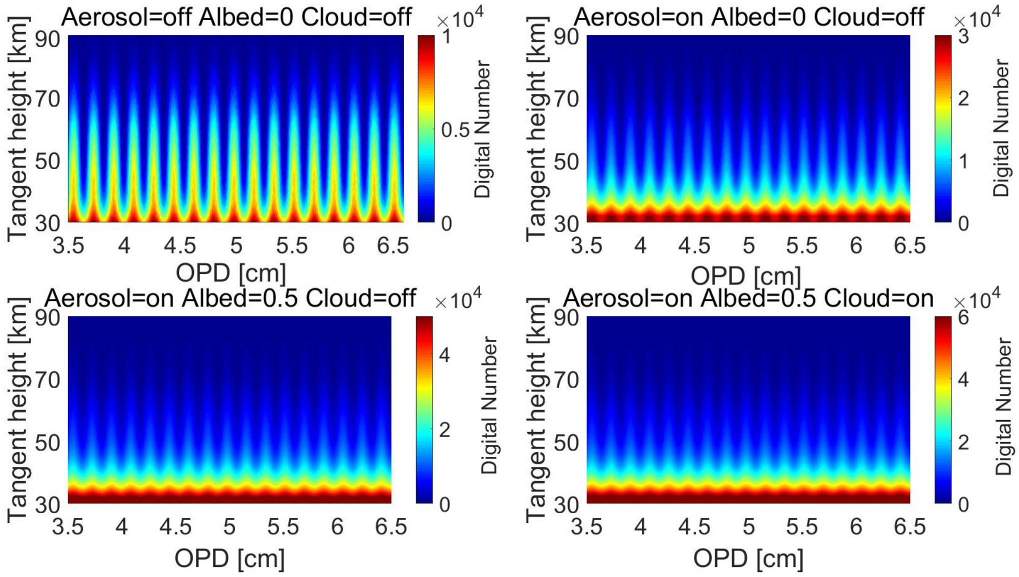

Figure 12. The variations of the combined signal images with aerosol, albedo, and cloud.

The sensitivity functions for the simulated interferogram images were determined for each OPD (corresponding to points along the horizontal axis of the interferogram image). Retrieval precisions were estimated from the sensitivity functions by combining observations from all OPD values, assuming a constant tangent height along each row. Statistically averaging of the columns of the pixel map provided the resultant wind profiles [31]. The corresponding wind error levels were also obtained at the same time, which are shown in Figure 13. This indicates that the random errors for Doppler wind were in the range of 2–3 m/s for the tangent height range from 45–80 km. The large values of wind error at higher tangent heights were because of the low effective SNR at those heights. The wind precision under 45 km suffered significantly from the scattered sunlight background. For a satellite-borne instrument to provide useful wind information, it needs to measure wind speed of at least a few meters per seconds. If the error level of 10 m/s for wind measurement is acceptable, a lower limit of 35 km in detection altitude can be achieved in the case of pure Rayleigh scattering. For the case of taking the atmospheric aerosol into account, this lower limit of detection altitude increased to 38 km. This value will reach 40 km in cloudy weather. This behavior is due to the fact that the shot noise depends largely on the scattered sunlight background, and the change of the surface albedo, aerosol loading, or cloud will inevitably lead to the variation of the effective SNR, which subsequently affects the wind precision.

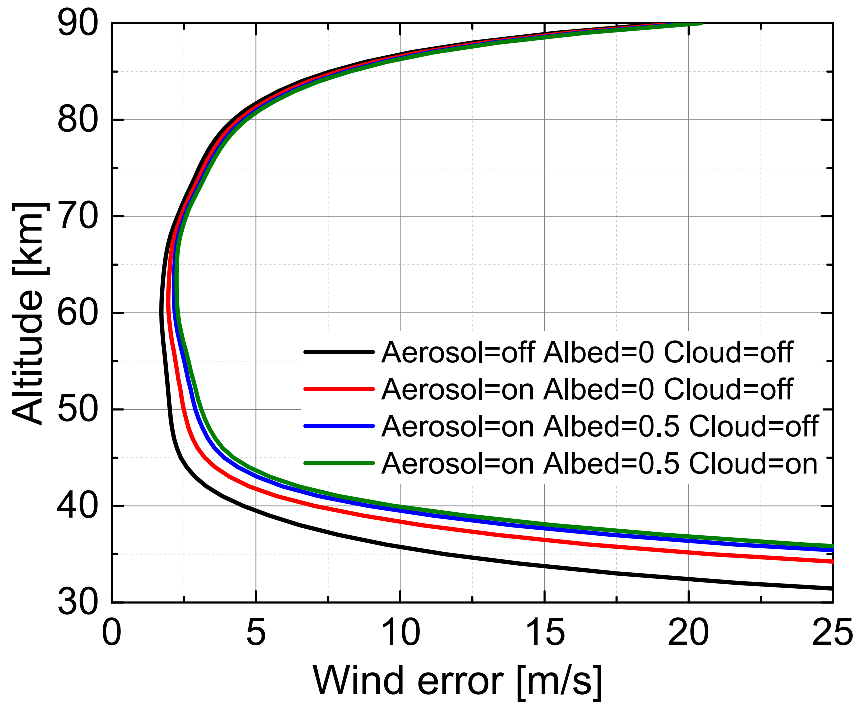

Figure 13. The variations of calculated wind precision profiles with aerosol, albedo, and cloud from 30 to 90 km.

5. Discussion

The sensitivity analyses can also be used to evaluate the influence of the variation of the system parameters on the wind measurements. The proper configuration of these parameters must meet the science objective within technology limitations and cost constraints. Here, the sensitivity of wind measurements to the Full-Width at Half-Maximum (FWHM) of the filter was investigated. Figure 14 shows the wind errors as a function of the filter FWHM for different tangent heights. As expected, the wind error decreased with the narrowing of the filter bandwidth. This behavior was more obvious for wind measurement at low altitudes. The wind error at 35 km was about 42 m/s with a filter bandwidth of 2 nm, and this value can be reduced to less than 10 m/s if a 0.1 nm FWHM bandwidth filter is used.

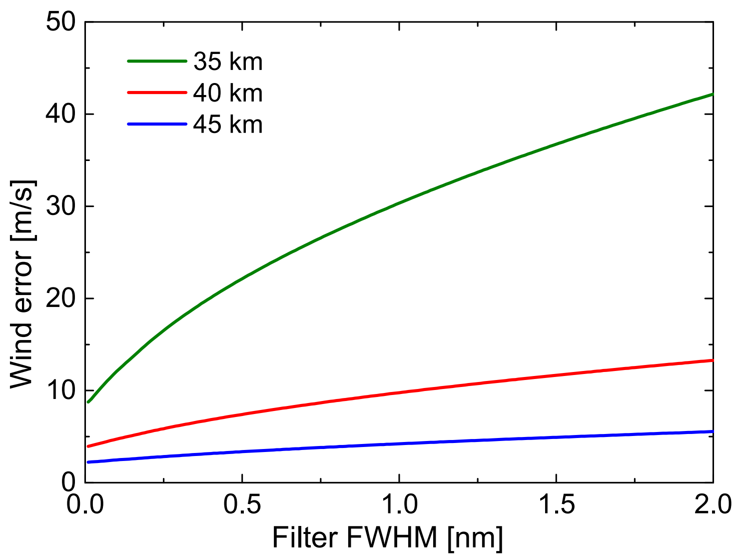

Figure 14. The wind errors as a function of filter FWHM for different tangent heights.

It can be advantageous to choose a very narrow band transmittance window positioned directly on the $O_{19}P_{18}$ emission line, as the wind sensitivity will be high and the noise reduction process becomes simpler. However, the central wavelength of the transmittance window of an ultra-narrow band interference filter changes obviously if the filter is not illuminated perpendicularly. Usually, the transmittance window shifts towards lower wavelengths as the illumination angle increases. As a result, each pixel filter passband will change, and this change will cause a phase shift in the interferogram. Furthermore, the maximum transmittance decreases, and the transmission bandwidth of the filter increases slightly, which will cause a contribution change of the atmospheric scattering background signal for different pixels. Thus, the dependence of the filter transmittance on the illumination angle can change the sensitivity of the Doppler shift of the emission line and will have a significant influence on wind measurement. In addition, ultra-narrow band interference filter with an FWHM less than 1 nm will also increase the engineering cost and implementation difficulty. With the comprehensive consideration of the balance in measurement requirements with technology limitations, the broad optimum was found to be a bandwidth around 1 nm for the limb-viewing DASH instrument. The peak transmittance of this 1 nm-wide filter is greater than 60%, and its out-of-band rejection ratio needs to be better than 10^3.

For a given value of the filter bandwidth, such as 1 nm, the detection accuracy of the limb-viewing DASH instrument depends very much on the SZA. Clearly, the SZA is the factor dominating the spectral brightness of both the atmospheric scattering and airglow emission. In Figure 15, the relative limb radiation of both the airglow emission and atmospheric scattering varying with the SZA for the tangent height at 40 km is displayed. As illustrated, the smaller the SZA, the brighter the airglow emissivity is, as well as the scattering rate. The slope of the scattering curve reduces as the SZA increases, while, the emission curve shows the opposite trend. This is expected since the UV photo-dissociation of O_3 penetrates more deeply when the SZA is small, which makes the airglow peak increase with the values of the SZA.

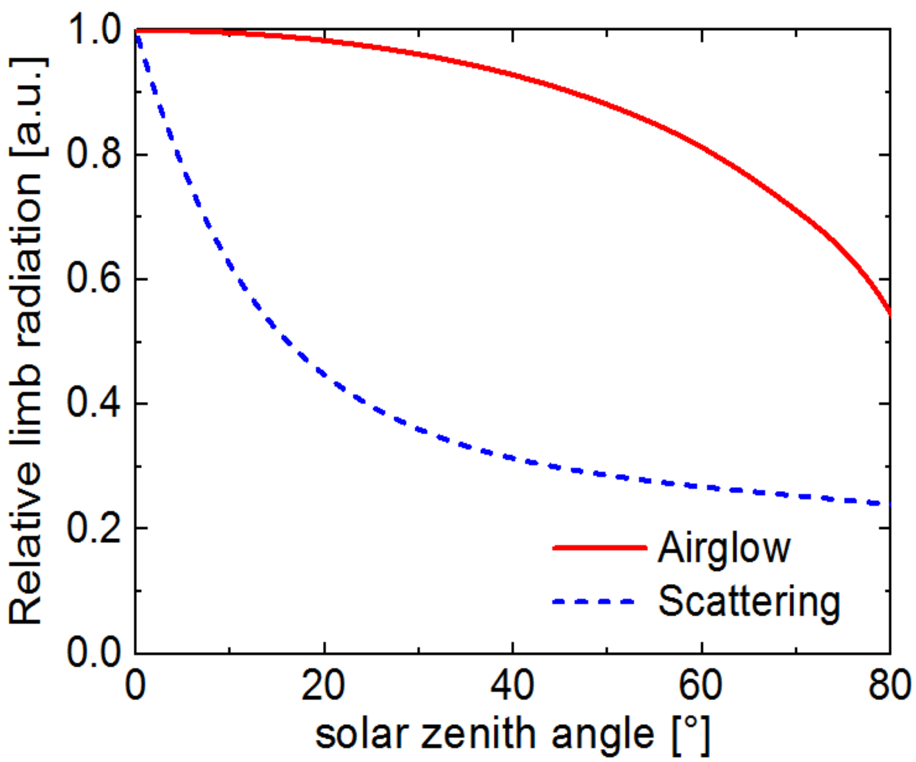

Figure 15. The relative limb radiation of both the airglow emission and atmospheric scattering varying with the SZA for a tangent height at 40 km.

Figure 16a shows the limb-viewing weight, as well as the emission contribution rate as a function of the SZA for a tangent height at 40 km. As the SZA increases, the weight of the target layer referring to the airglow monotonically decreases, while the emission contribution rate, which is defined as ratio of the intensity between the airglow and scattering, demonstrates a parabolic curve with a peak at about SZA = 50°. This behavior is due to the fact that we are looking at smaller scattering angles as the SZA increases. It is important to note that the scattering brightness for the case of an overhead Sun is quite sensitive to changes in the surface albedo. As the SZA increases, the simulations correspond to a smaller scattering angle, and the subsequent increase in intensity masks any changes due to the albedo variation. Figure 16b displays the wind error at different values of the SZA for a tangent height at 40 km. The wind error fluctuates within a narrow range between 6 m/s and 8 m/s for SZA variations from 0° to 60° and increases sharply when the SZA is larger than 70°. This is expected since the altitude of the main airglow emissivity peak increases for higher values of the SZA.

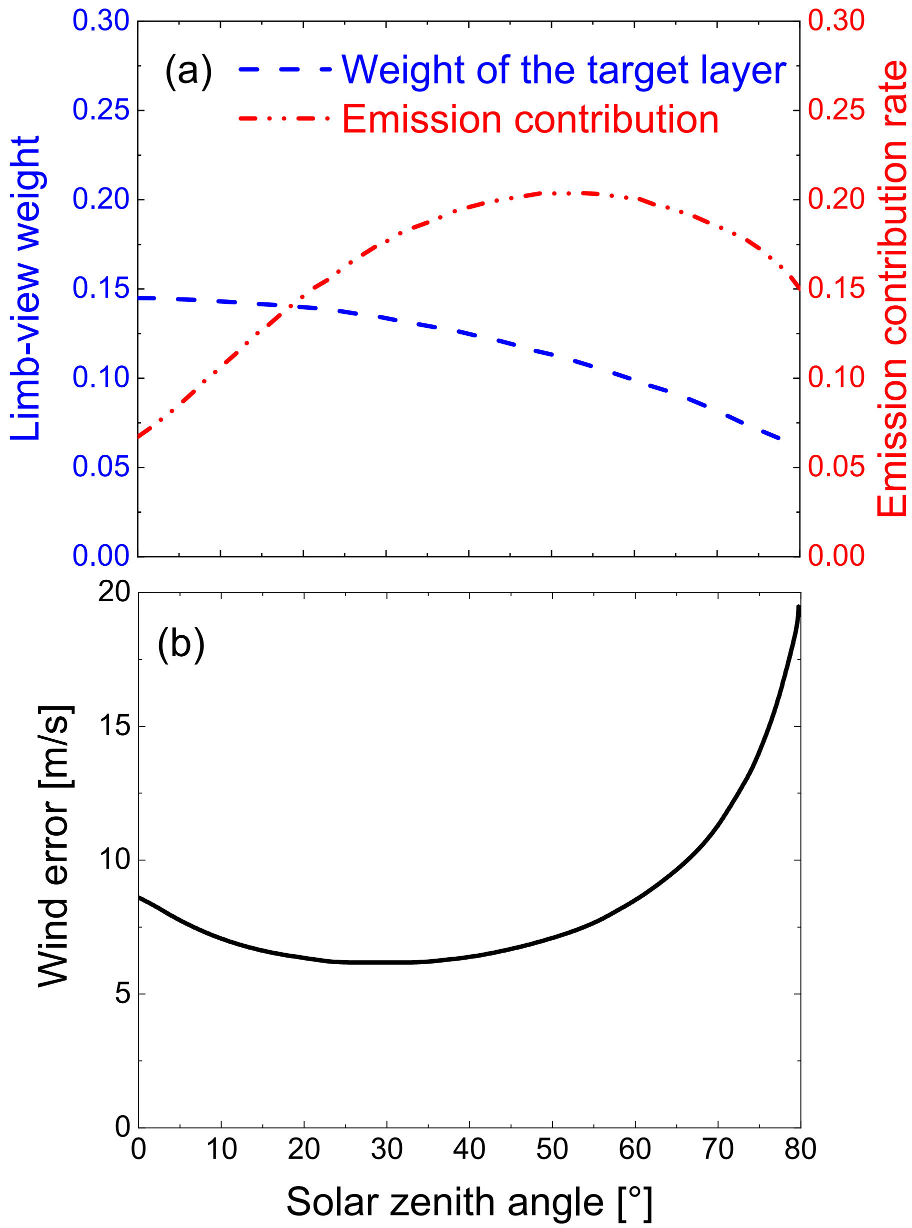

Figure 16. (**a**) The limb-viewing weight, as well as the emission contribution rate as a function of the SZA for a tangent height at 40 km; (**b**) the wind error at different values of the SZA.

6. Conclusions

We discussed the influence of scattered sunlight on wind measurements by observing the $O_2(a^1\Delta_g)$ dayglow with a limb-viewing DASH instrument. Observing the Doppler shift of the emission line $O_{19}P_{18}$ (7772.030 cm^{-1}) allows high-precision and high-sensitivity wind speed measurements in the space area of 40–80 km and is therefore well suited to fill the vacancy in the altitude region where the newest space-borne sensors (ADM-Aeolus and MIGHTI) have no competence to probe. However, it also suffers serious spectral interference from the scattered sunlight background, which previous wind imaging interferometers (such as WINDII and TIDI) were spared. The infrared atmospheric band can be observed both in emission and absorption, and the surface albedo, aerosol loading, and cloud have a significant influence on the radiative transfer characteristics of the $O_2(a^1\Delta_g)$ band in limb-viewing geometry. Based on the atmospheric limb radiance spectra and the instrument concept of the limb-viewing DASH, the corresponding interferogram images were simulated. We described how to remove the atmosphere-scattering component to generate a pure airglow interferogram and how to retrieve the interferogram containing information solely from the target altitude by unraveling the LOS integration with the self-absorption process of O_2 molecules being taken into account. The presence of the scattered sunlight decreases the interferogram contrast and increases the measurement noise, which affect the limb-viewing weight and effective SNR adversely. This work demonstrated that the measurement precision of Doppler wind is about 2–3 m/s at the tangent height range from 45–80 km and suffers significantly from scattered sunlight background under 45 km. For an acceptable error level of 10 m/s, the lower limit of detection altitude is about 35 km in the case of pure Rayleigh scattering and increases to 40 km in cloudy weather.

We discussed the relationship between the filter FWHM and wind precision and presented the optimum bandwidth for this limb-viewing DASH instrument based on the consideration of the balance between measurement precision and engineering difficulty. Furthermore, we also discussed the wind errors varying with the SZA. The wind error fluctuates within a narrow range between 6 m/s and 8 m/s for SZA variations from 0° to 60°, and increases sharply when the SZA is larger than 70° for a tangent height at 40 km.

In future work, we will focus on solving the technical problem of wind inversion error caused by atmospheric refraction in low-altitude areas. Through comprehensively considering the influence of atmospheric scattering and refraction, the forward simulation in low-altitude areas will be more accurate and the wind inversion error will be further reduced.

Author Contributions: Conceptualization, W.H. and K.W.; methodology, K.W., W.H. and F.L.; software, K.W., D.W. and J.L.; investigation, X.H. and J.L.; visualization, K.W. and H.W.; writing—original draft preparation, W.H. and K.W.; writing—review and editing, F.L., X.H. and K.W.; supervision, F.L. and D.W.; funding acquisition, K.W., W.H. and F.L. All authors have read and agreed to the published version of the manuscript.

Funding: This research was funded by the National Natural Science Foundation of China (41975039, 61705253), the Natural Science Foundation of Shandong Province (ZR2021QD088), the Youth Innovation Technology Project of Higher School in Shandong Province (2021KJ008), and the National Key R&D Program of China (2017YFC0211900).

Data Availability Statement: The data presented in this study are available upon request from the corresponding author.

Acknowledgments: The authors gratefully acknowledge helpful and informative discussions with Wang Dingyi on the theoretical details of this work.

Conflicts of Interest: The authors declare no conflict of interest.

References

1. Bauer, P.; Thorpe, A.; Brunet, G. The quiet revolution of numerical weather prediction. *Nature* **2015**, *525*, 47–55. [CrossRef] [PubMed]
2. Han, Y.L.; Sun, D.S.; Han, F.; Liu, H.A.; Zhao, R.C.; Zhen, J.; Zhang, N.N.; Chen, C.; Li, Z.M. Demonstration of daytime wind measurement by using mobile Rayleigh Doppler Lidar incorporating cascaded Fabry-Perot etalons. *Opt. Express* **2019**, *27*, 34231–34247. [CrossRef] [PubMed]
3. Dabas, A. Observing the atmospheric wind from space. *Cr. Geosci.* **2010**, *342*, 370–379. [CrossRef]
4. Baumgarten, G. Doppler Rayleigh/Mie/Raman lidar for wind and temperature measurements in the middle atmosphere up to 80 km. *Atmos. Meas. Tech.* **2010**, *3*, 1509–1518. [CrossRef]
5. Ruf, C.S.; Atlas, R.; Chang, P.S.; Clarizia, M.P.; Garrison, J.L.; Gleason, S.; Katzberg, S.J.; Jelenak, Z.; Johnson, J.T.; Majumdar, S.J.; et al. New Ocean Winds Satellite Mission to Probe Hurricanes and Tropical Convection. *Bull. Amer. Meteor. Soc.* **2016**, *97*, 385–395. [CrossRef]
6. Mitra, A.K.; Kundu, P.K.; Giri, R.K. A quantitative analysis of KALPANA-1 derived water vapor winds and its impact on NWP model. *Meteorol Atmos. Phys.* **2013**, *120*, 29–44. [CrossRef]
7. Savli, M.; de Kloe, J.; Marseille, G.J.; Rennie, M.; Zagar, N.; Wedi, N. The prospects for increasing the horizontal resolution of the Aeolus horizontal line-of-sight wind profiles. *Q. J. Roy. Meteor. Soc.* **2019**, *145*, 3499–3515. [CrossRef]
8. Englert, C.R.; Harlander, J.M.; Brown, C.M.; Marr, K.D.; Miller, I.J.; Stump, J.E.; Hancock, J.; Peterson, J.Q.; Kumler, J.; Morrow, W.H.; et al. Michelson Interferometer for Global High-Resolution Thermospheric Imaging (MIGHTI): Instrument Design and Calibration. *Space. Sci. Rev.* **2017**, *212*, 553–584. [CrossRef]
9. Marr, K.D.; Morrow, W.H.; Brown, C.M.; Englert, C.R.; Harandert, J.M.; Cerrato, A.; Lamport, K.; Harris, S.E. Cal-ibration lamp design, characterization, and implementation for the Michelson Interferometer for Global High-Reso-lution Thermospheric Imaging instrument on the Ionospheric Connection satellite. *Opt. Eng.* **2019**, *58*, 054104. [CrossRef]
10. Rahnama, P.; Gault, W.; McDade, I.; Shepherd, G. Design requirements for the SWIFT instrument. *Meas. Sci. Technol.* **2013**, *24*, 015801. [CrossRef]
11. Gordley, L.L.; Marshall, B.T. Doppler wind and temperature sounder: New approach using gas filter radiometry. *J. Appl. Remote Sens.* **2011**, *5*, 053570. [CrossRef]
12. Ward, W.E.; Gault, W.A.; Shepherd, G.G.; Rowlands, N. The Waves Michelson Interferometer: A visible/near-IR interferometer for observing middle atmosphere dynamics and constituents. *Sens. Syst. Next-Gener. Satell. V* **2001**, *4540*, 100–111. [CrossRef]
13. Wu, K.; Fu, D.; Feng, Y.; Li, J.; Hao, B.; Li, F. Simulation and application of the emission line $O_{19}P_{18}$ of $O_2(a^1\Delta g)$ day-glow near 1.27 µm for wind observations from limb-viewing satellites. *Opt. Express* **2018**, *26*, 16984–16999. [CrossRef] [PubMed]
14. Shepherd, G.G.; Thuillier, G.; Cho, Y.M.; Duboin, M.L.; Evans, W.F.J.; Gault, W.A.; Hersom, C.; Kendall, D.J.W.; Lathuillere, C.; Lowe, R.P.; et al. The Wind Imaging Interferometer (WINDII) on the Upper Atmosphere Research Satellite: A 20 Year Perspective. *Rev. Geophys.* **2012**, *50*, 2. [CrossRef]
15. Zhang, J.; Forbes, J.M. Lunar tidal winds between 80 and 110 km from UARS/HRDI wind measurements. *J. Geophys. Res. Space Phys.* **2013**, *118*, 5296–5304. [CrossRef]
16. Killeen, T.L.; Wu, Q.; Solomon, S.C.; Ortland, D.A.; Skinner, W.R.; Niciejewski, R.J.; Gell, D.A. TIMED Doppler interferometer: Overview and recent results. *J. Geophys. Res. Space Phys.* **2006**, *111*, A10. [CrossRef]
17. He, W.; Wu, K.; Feng, Y.; Fu, D.; Chen, Z.; Li, F. The Radiative Transfer Characteristics of the O_2 Infrared Atmospheric Band in Limb-Viewing Geometry. *Remote Sens.* **2019**, *11*, 2702. [CrossRef]
18. Yankovsky, V.; Manuilova, R.; Babaev, A.; Feofilov, A.; Kutepov, A. Model of electronic-vibrational kin-etics of the O_3 and O_2 photolysis products in the middle atmosphere: Applications to water vapour retrievals from S-ABER/TIMED 6.3 µm radiance measurements. *Int. J. Remote Sens.* **2011**, *32*, 3065–3078. [CrossRef]
19. Yankovsky, V.A.; Martyshenko, K.V.; Manuilova, R.O.; Feofilov, A.G. Oxygen dayglow emissions as proxies for a-tomic oxygen and ozone in the mesosphere and lower thermosphere. *J. Mol. Spectrosc.* **2016**, *327*, 209–231. [CrossRef]
20. Martyshenko, K.V.; Yankovsky, V.A. IR Band of O_2 at 1.27 µm as the Tracer of O_3 in the Mesosphere and L-ower Thermosphere: Correction of the Method. *Geomagn. Aeron.* **2017**, *57*, 229–241. [CrossRef]
21. Emmert, J.T.; Drob, D.P.; Picone, J.M.; Siskind, D.E.; Jones, M.; Mlynczak, M.G.; Bernath, P.F.; Chu, X.; Doornbos, E.; Funke, B.; et al. NRLMSIS 2.0: A Whole-Atmosphere Empirical Model of Temperature and Neutral Species Densities. *Earth Space Sci.* **2021**, *8*, e2020EA001321. [CrossRef]
22. Berk, A.; Conforti, P.; Kennett, R.; Perkins, T.; Hawes, F.; van den Bosch, J. MODTRAN (R) 6: A major upgrade of the MODTRAN (R) radiative transfer code. *Algorithms Technol. Multispectral Hyperspectral Ultraspectral Imag. Xx* **2014**, *9088*, 1–4. [CrossRef]
23. Yee, J.H.; DeMajistre, R.; Morgan, F. The $O_2(b^1\Sigma)$ dayglow emissions: Application to middle and upper atmosphere remote sensing. *Can. J. Phys.* **2012**, *90*, 769–784. [CrossRef]
24. Yankovsky, V.A.; Babaev, A.S. Photolysis of O_3 at Hartley, Chappuis, Huggins, and Wulf bands in the middle atmo-sphere: Vibrational kinetics of oxygen molecules $O_2(X^3\Sigma g-, \nu \leq 35)$. *Atmos. Ocean. Opt.* **2011**, *24*, 6–16. [CrossRef]
25. Englert, C.R.; Babcock, D.D.; Harlander, J.M. Doppler asymmetric spatial heterodyne spectroscopy (DASH): Concept and experimental demonstration. *Appl. Opt.* **2007**, *46*, 7297–7307. [CrossRef] [PubMed]
26. Englert, C.R.; Harlander, J.M.; Emmert, J.T.; Babcock, D.D.; Roesler, F.L. Initial ground-based thermospheric wind measurements using Doppler asymmetric spatial heterodyne spectroscopy (DASH). *Opt. Express* **2010**, *18*, 27416–27430. [CrossRef]

27. Harding, B.J.; Makela, J.J.; Englert, C.R.; Marr, K.D.; Harlander, J.M.; England, S.L.; Immel, T.J. The MIGHTI Wind Retrieval Algorithm: Description and Verification. *Space Sci. Rev.* **2017**, *212*, 585–600. [CrossRef]
28. Drob, D.P.; Emmert, J.T.; Meriwether, J.W.; Makela, J.J.; Doornbos, E.; Conde, M.; Klenzing, J.H. An update to the Horizontal Wind Model (HWM): The quiet time thermosphere. *Earth Space Sci.* **2015**, *2*, 301–319. [CrossRef]
29. Wu, Y.J.J.; Harding, B.J.; Triplett, C.C.; Makela, J.J.; Marr, K.D.; Englert, C.R.; Harlander, J.M.; Immel, T.J. Errors From Asymmetric Emission Rate in Spaceborne, Limb Sounding Doppler Interferometry: A Correction Algorithm With Application to ICON/MIGHTI. *Earth Space Sci.* **2020**, *7*, e2020EA001164. [CrossRef]
30. Liu, J.; Wei, D.; Zhu, Y.; Kaufmann, M.; Olschewski, F.; Mantel, K.; Xu, J.; Riese, M. Effective wind and temperature retrieval from Doppler asymmetric spatial heterodyne spectrometer interferograms. *Appl. Opt.* **2018**, *57*, 8829–8835. [CrossRef]
31. Harlander, J.M.; Englert, C.R.; Marr, K.D.; Harding, B.J.; Chu, K. On the uncertainties in determining fringe phase in Doppler asymmetric spatial heterodyne spectroscopy. *Appl. Opt.* **2019**, *58*, 3613–3619. [CrossRef] [PubMed]